RSC Advances

PAPER

View Article Online
View Journal | View Issue

Check for updates

Cite this: *RSC Adv.*, 2025, **15**, 30415

UV-blocking and mechanically reinforced starch films incorporating Ce-UiO-66 nanoparticles for food packaging applications

Giang H. Le, *[ab] Duong A. Thanh,[a] Trang T. T. Pham,[a] Quang Vinh Tran,[ab] Nhiem Ngoc Dao,[bc] Kien Trung Nguyen, [c] Són Tung Pham[a] and Trang T. T. Quan *[a]

Received 3rd May 2025
Accepted 20th August 2025

DOI: 10.1039/d5ra03117f

rsc.li/rsc-advances

Hazardous ultraviolet (UV) radiation found in sunlight can seep into food packaging and cause unfavorable physicochemical changes in food items. This study aimed to develop starch-based polymeric biofilms with UV-blocking capability by incorporating CeUiO-66 metal–organic framework nanoparticles (Ce66 NPs). These nanoparticles were synthesized *via* a solvothermal method using formic acid as a modulator. A Box–Behnken design was used to optimize modulator concentration, reaction temperature, and time to maximize surface area and yield. Under optimal conditions, Ce66 NPs exhibited high crystallinity, an average particle size of 287 nm, a large surface area (832.20 m^2 g^{-1}), and a yield of 66.25%. The Ce66 NPs were incorporated into starch films (SCe*x*, $x = 0.5$–3.0 wt%) *via* solution casting using glycerol as a plasticizer in an acetic acid medium. Although the addition of Ce66 NPs reduced film transparency, it significantly improved UV-blocking efficiency. Specifically, the SCe1 film blocked 83.5% UVA, 95.6% UVB, and 100% UVC radiation. Water vapor permeability decreased to 1.69 g mm m^{-2} d^{-1} kPa^{-1}, and solubility dropped to one third compared to the control film. The tensile strength also increased from 2.2 MPa to 8.4 MPa. Moreover, Ce66 NPs exhibited notable photocatalytic activity, degrading up to 65% of RR195 dye under visible light. This dual functionality underscores the potential of Ce66 NPs for developing multifunctional biofilms for food packaging and environmental treatment.

1. Introduction

Conventional plastics are made from synthetic polymers derived from petroleum and are widely used due to their advantages such as high mechanical durability, low cost, and ease of synthesis.[1] However, they are non-biodegradable, causing secondary pollution and negatively impacting the environment and ecosystems.[2] As a result, there is a growing trend toward seeking new materials that are recyclable, biodegradable, and environmentally friendly, such as bioplastics derived from starch,[3] chitosan,[4] cellulose,[5] gelatin, and plant-based proteins,[6] *etc.* Despite their advantages, biopolymer based films often suffer from inherent drawbacks including poor mechanical strength, high water solubility, and limited barrier properties. Therefore, many researchers have incorporated inorganic nanomaterials as reinforcing fillers into biopolymer matrices to improve the final material properties in a beneficial manner.[3,7]

Nanoparticles such as silver, ZnO, TiO_2, CuO, graphene oxide, carbon nanoparticles, and bentonite nanoparticles are considered promising candidates for reinforcing biopolymer films, as they not only enhance characteristics like biocompatibility, tensile strength, Young's modulus, and thermal stability but also improve the light-barrier properties of the resulting films.[8,9] Recently, metal–organic frameworks (MOFs) have emerged as materials with high specific surface area, gas barrier properties, good thermal stability, and excellent compatibility with biopolymers, making them suitable additives for developing biofilms with novel functionalities.[10–14]

Several studies have demonstrated the potential of MOFs in biofilm enhancement. Akash Balakrishnan[15] incorporated MOFs into chitosan films for use in food packaging and catalysis. Sanjit Nayak[16] employed a zirconium-based MOFs and polycaprolactone (PCL) to create a material capable of controlled release of the herbicide 2-methyl-4-chlorophenoxyacetic acid (MCPA), offering a promising avenue for agricultural applications. Naveed Ahmed Khan[10] developed food packaging films by combining ZIF-67 with PVA/starch, and the addition of 4.0 wt% ZIF-67 resulted in a biopolymer film with a mechanical strength of up to 25 MPa

---

[a] Institute of Chemistry, Vietnam Academy of Science and Technology, 18 Hoang Quoc Viet, Cau Giay, Hanoi 100000, Vietnam. E-mail: giangnasa86@gmail.com; quanthutrang5986@gmail.com

[b] Graduate University of Science and Technology, Vietnam Academy of Science and Technology, 18 Hoang Quoc Viet, Cau Giay, Hanoi 100000, Vietnam

[c] Institute of Material Science, Vietnam Academy of Science and Technology, 18 Hoang Quoc Viet, Cau Giay, Hanoi 100000, Vietnam

and enhanced thermal resistance. L. Sun[13] used MIL-125(Ti)-NH_2 nanoparticles with cellulose to fabricate biopolymer films with UV shielding capability and a 25.9% increase in mechanical strength. The flame resistance was notably significantly improved, with the limiting oxygen index (LOI) rising from 21.95% to 27.01% in the presence of MIL-125(Ti)-NH_2 nanoparticles.

Among MOFs, cerium-based MOFs (Ce-MOFs) are particularly attractive due to their cost-effective synthesis, high chemical and thermal stability, and redox-active Ce^{3+}/Ce^{4+} sites. These properties make Ce-MOFs suitable for applications in catalysis, corrosion protection, and energy storage.[17] Typically, terephthalic acid (H_2BDC) and its derivatives are used to synthesize various Ce-MOFs, such as CeUiO-66, with the formula $Ce_6O_4(OH)_4(BDC)_6$, which exhibits high stability and thermal endurance up to 300 °C.[18,19] However, the synthesis of nano-sized Ce-MOFs remains challenging, particularly in controlling particle size, porosity, and yield.[19] It is well known that synthesis parameters including modulator type and concentration, temperature, and reaction time can profoundly affect the morphology and properties of MOFs.[20] During synthesis, carboxylic acids with varying pKa values act as modulators, influencing the size and surface area of the resulting MOFs depending on their dosage.[21] Additionally, reaction temperature and time are critical factors affecting crystal formation and growth. Elevated temperatures significantly promote crystal restructuring and Ostwald ripening.[22] When the reaction time is prolonged, MOFs crystals tend to evolve into more stable forms with well defined facets under the guidance of facet specific protective agents.[23] Further extension of reaction time may induce crystal restructuring and Ostwald recrystallization, potentially affecting the properties of the final MOFs product.[22–24]

Response Surface Methodology (RSM) is an important technique used to optimize processes. The Box–Behnken Design (BBD), which requires fewer experiments while accurately modeling higher order interactions, has been successfully applied in various fields, including the optimization of film thickness, nanocomposite material synthesis, and mechanical, thermal, and optical property enhancement.[25,26]

To address these gaps, our study aims to: (1) optimize the solvothermal synthesis of CeUiO-66 nanoparticles (Ce66 NPs) using RSM and BBD to maximize surface area and yield; and (2) incorporate Ce66 NPs into starch based biopolymer films to evaluate their effects on physicomechanical and optical performance. Notably, we demonstrate for the first time the use of Ce66 NPs in enhancing UV-blocking efficiency and mechanical strength of starch films, while also serving as visible light photocatalysts for degradation of the azo dye RR195, a common pollutant in textile wastewater. This dual functionality highlights the potential of Ce66 NPs for both environmental treatment and development of advanced biopackaging materials.

Design Expert software (DXs) was employed to optimize the synthesis process of Ce66 NPs and to identify the most influential synthesis parameters using RSM. The optimized Ce66 NPs were subsequently characterized using XRD, SEM, BET, XPS, TGA, and UV-vis analyses. The physicomechanical properties of the biopolymer film samples containing Ce66 NPs were evaluated through tensile tests, water solubility (WS), water vapor permeability (WVP), transparency, and UV-blocking capability.

2. Material and methods

2.1. Chemical

For the synthesis of Ce66 NPs, the chemical ($(NH_4)_2Ce(NO_3)_6$, 99.99%) (denoted as CAN) was supplied by Adamas-beta (China). The reagents H_2BDC (99%), formic acid (FA, HCOOH, 98%), acetone (C_3H_6ON, 99.5%), and DMF (99.5%) were also sourced from China and were used directly without undergoing further purification.

To synthesis the biopolymer films, cassava starch (Vietnam, amylose content: 29%, moisture content: 12%) was modified before use. Hydrochloric acid (HCl, 36.5%), sodium hydroxide (NaOH, 98%), sodium bicarbonate ($NaHCO_3$, 99%), acetic acid (CH_3COOH, 99.5%), and glycerol ($C_3H_8O_3$, 99%) were purchased from China.

2.2. Synthesis of Ce66 NPs

To optimize the synthesis of Ce66 NPs focusing on enhancing surface area and the yield, a fixed reaction volume of 50 mL was maintained throughout all experimental trials. Specifically, 4.0 mL of 0.533 M CAN was gradually added from a 100 mL stock solution into the reaction vessel containing 12 mL of DMF, 354 mg of H_2BDC, and varying volumes of FA ranging from 1.0 to 19 mL. The addition rate of CAN was kept constant at 2 mL per minute, and the stirring speed was maintained at 400 rpm. Upon completion of the addition, the reaction mixture was stirred for an additional 15 minutes at room temperature. The reaction vessel was then transferred into a thermostatic system, where the temperature was set within the range of 60–120 °C. The reaction time was varied from 0.5 to 9.5 hours. At the end of the reaction, the resulting solid was collected by centrifugation using 50 mL Falcon tubes under fixed conditions (5500 rpm, 5 minutes per cycle) at room temperature, employing a Hettich UNIVERSAL 320 centrifuge. The washing process was repeated twice using a fixed solvent mixture of 25 mL H_2O, 25 mL DMF, and 25 mL acetone. The final product was dried at 90 °C for 6 hours to remove moisture. The yield was calculated based on the molar amount of Ce^{4+} salt, using eqn (1) provided in the SI. The DXs was employed to determine the optimal synthesis conditions *via* the RSM using the BBD.

2.3. Synthesis of biopolymer films

Cassava starch (30.0 g) was dispersed in a mixture of 160 mL of ethanol and water (9 : 1 by volume) and gently stirred. After stirring at 70 °C for 10 minutes, 7 mL of HCl 36.5% was added to the mixture. The reaction was carried out at 70 °C for 1 hour, and then 8.0 g of $NaHCO_3$ was added to stop the reaction. After cooling to room temperature, the solution was centrifuged at 5500 rpm for 5 minutes. The precipitate was washed four times with distilled water, followed by a fifth wash with ethanol, then dried at 70 °C in an oven for 12 hours. Next, 3.0 g of the modified starch was added to 80 mL of water and stirred at 90 °C to form sol A. Then, 30% glycerol, 20 mL of water, and 0.5–3.0% Ce66 NPs (by weight of starch) were ultrasonically treated at 20 kHz for 10 minutes to obtain sol B. Sol B was gradually added to sol A while stirring at 400 rpm for 0.5 hour until the mixture gelled. To prepare the starch based biopolymer films, 5 mL of acetic acid (5.0% v/v) was added to the formulation to maintain the pH of the film forming solution. The resulting solution was then cast onto polytetrafluoroethylene (PTFE) molds with fixed dimensions of 18.7 × 18.7 × 1.5 cm. The films were allowed to dry at ambient temperature (25 ± 2 °C) for 24 hours, followed by further drying in a ventilation oven at 50 °C for 6 hours to ensure complete removal of residual water. Once thoroughly dried, the films were carefully peeled off from the molds and conditioned in a desiccator maintained at 50% relative humidity for 48 hours before testing. Film samples were labeled according to the Ce66 NPs content: SCe0 (0 wt% Ce66 NPs, control), SCe05 (0.5 wt%), SCe1 (1.0 wt%), and SCe3 (3.0 wt%).

2.4. Morphological characterization of the material

The nitrogen adsorption–desorption method at 77.350 K was used to determine the surface area. Before measurement, the Tristar II Plus system was calibrated using a standard silica-alumina sample (LOT: A-501-64, micromeritics). The sample treatment was performed at 150 °C for 6 hours with a sample mass of 0.3 g and an equilibration interval of 10 seconds. Scanning Electron Microscopy (SEM) measurements were conducted using the Hitachi S-4800 under the following conditions: accelerating voltage of 10.0 kV, working distance of 9.7 mm, and emission current of 9.4 nA. The valence state and chemical bonding of Ce66 NPs were analyzed using X-ray Photoelectron Spectroscopy (XPS) on a Thermo vg scientific (U.K.) MultiLab 2000 machine. X-ray Diffraction (XRD) was performed on a D8-Advance machine with CuK$_\alpha$ radiation ($\lambda = 1.5406$ Å). Thermogravimetric Analysis (TGA) was carried out on a Labsys Evo TG-DTA machine (Setaram, France) with a heating rate of 5 °C per minutes. The properties of the biodegradable films, such as water solubility, film thickness, and UV-blocking ability in the azo dye RR195 degradation reaction, are described in the SI.

2.5. Characterization of synthesized SCe*x* films properties

2.5.1. Tensile strength. Tensile strength was determined according to ASTM D882 using a universal testing machine (Instron 5980) at a crosshead speed of 10 mm per minute. Samples were cut into dumbbell shapes (dimensions: 25 × 110 mm). Each measurement was repeated three times per sample.

2.5.2. Water vapor permeability (WVP). The water vapor permeability (WVP) of the films was determined following ASTM E96-00 and the method described by Sakshi Dhiman *et al.*,.[27] Forty grams of silica gel (0% RH), pre-dried in an oven at 120 °C for 24 hours, was placed into fixed-diameter test cups, maintaining a 1.0 cm gap between the film and silica gel layer. The cups were then sealed with the test films and placed in a desiccator maintained at 75% RH and 25 °C. The cups were weighed every 24 hours for one week, with weight recorded to an accuracy of 0.0001 g. The WVP value was calculated using eqn (1):

$$\mathrm{WVP} = \frac{W \times d}{t \times A \times \Delta P} \tag{1}$$

where: $\Delta P$is the water vapor pressure difference at 25 °C (kPa) between the interior and exterior of the cup, A is the area of the film exposed to vapor transmission (m^2), t is the testing time (day), W is the mass of water vapor transmitted through the film (g), d is the film thickness (mm).

2.5.3. UV-blocking properties, transparency, and opacity tests. The transparency (T%) was estimated based on the transmittance value at a wavelength of 600 nm using a UV-vis spectrophotometer (Shimadzu, UV 1900, Tokyo, Japan). Rectangular samples with dimensions of 10 mm × 40 mm and fixed thickness were placed in a quartz cuvette. An empty quartz cuvette was used as the ref. 1 and 28.

The opacity (mm^{-1}) was calculated using the formula eqn 2 in the SI.[27]

The ability to block UVA, UVB, and UVC radiation was determined based on the transmittance values analyzed over the 200–800 nm wavelength range. Specifically, UVA was calculated for the wavelength range of 315–400 nm, UVB for 280–315 nm, UVC for 200–280 nm, and blue light for the wavelength range of 400–495 nm, following the formulas eqn 3 to eqn 6 (SI).[1]

3. Results and discussions

3.1. Optimization of Ce66 NPs synthesis process using RSM-BBD method

The BBD method for second order optimization is presented in Table S1, which is used to design the matrix for 15 experimental runs with three repetitions at the center. In this, the amount of modifier FA (FA) is examined in the range of 1.0–19 mL, reaction temperature from 60 to 120 °C, and reaction time is investigated from 0.5 to 9.5 hours. The experimental results of the 15 trials and predictions by the DXs software are shown in Table S2. According to the results in Table S2, the statistical model represents the dependency of surface area (S) and the yield (H) on the independent variables temperature, time, and FA, following a second order equation in the coded form as follows:

$$\begin{aligned} S = {} & 742.42 - 213.61A - 83.88B + 38.46C \\ & + 250.49AB + 78.06AC - 169.97BC \\ & - 102.53A^2 - 260.49B^2 - 244.76C^2 \end{aligned} \tag{2}$$

$$\begin{aligned} H = {} & 62.24 + 2.15A + 15.26B + 5.05C \\ & - 0.9650AB - 3.39AC - 3.16BC \\ & + 3.87A^2 - 22.45B^2 - 2.59C^2 \end{aligned} \tag{3}$$

The selected values presented in eqn (2) and (3) were determined through the analysis of variance (ANOVA) in Table S3, using a significance threshold of $P < 0.05$. The positive and negative signs of each coefficient indicate the contributing effect of each factor in the model about the H and S of the resulting material. Accordingly, the more positive or more negative the value, the greater its impact, and *vice versa*.[25]

For the target function S, all three factors FA, time, and temperature, exhibited a significant influence on the surface area following a second-order model with negative coefficients (-102.53, -260.49, and -244.76, respectively). Notably, FA and temperature, exerted a strong influence on S with a higher positive interaction coefficient (250.49) compared to the interactions of FA/time and temperature/time. Regarding the target function H, both FA and temperature had a strong positive impact on the yield, with second order coefficients of 3.87 and 22.45, respectively. Furthermore, the FA/time and temperature/time interactions also significantly affected the yield. As shown in Table S3, the FA and temperature were the most influential factors on the H. Conversely, for the surface area, temperature and reaction time played the most critical roles.

The influence of various factors on the surface area and the yield in the synthesis of Ce66 NPs is illustrated by three-dimensional (3D) response surface plots (Fig. 1). In these plots, the red zones represent the highest desirable values, while the blue zones indicate lower results. As shown in Fig. 1a, a high concentration of FA acid suppresses the crystallization process, thereby inhibiting particle formation and reducing the surface area during MOFs synthesis.[29] The analysis of Fig. 1b confirms that increases in both temperature and time significantly decreases the surface area of the material due to excessive crystal growth of the MOFs. Furthermore, a prolonged time may lead to particle aggregation, resulting in a lower the yield, as illustrated in Fig. 1c. These observations are consistent with the findings reported by Antonietta Mancuso *et al.*.[20] From the analysis of Fig. 1, it is evident that the highest synthesis efficiency is achieved under conditions of low FA, short reaction time, and moderate temperature. The optimal synthesis conditions for gaining a high surface area and the yield of Ce66 NPs were determined using DXs. The optimal point, including FA, temperature, and time values, is listed in Table S4, with a maximum desirability of 0.990. Under these optimized conditions, the resulting surface area reached 832.20 $m^2\ g^{-1}$, and the yield was 66.25%, with no significant difference at the 95% confidence level between the predicted and experimental values. These results confirm the success of the applied model in optimizing the synthesis process of Ce66 NPs.

Fig. 2 presents the agreement between experimental and predicted values, along with residual plots, for S and H in 15 runs, confirming model reliability. The data presented in Fig. 2a and c further indicate that the model demonstrates a strong correlation, as the data points are closely aligned along a straight line. The response plots of experimental *versus* predicted values reveal minimal deviation between the values (Fig. 2b and d). The low coefficient of variation (CV%): 6.05% for S and 3.94% for H indicates the high reliability of the experimental data. The model's adequacy was evaluated through the adjusted R^2 and predicted R^2 coefficients, with a difference of less than 0.2 indicating the accuracy and significance of the proposed models (Table S5). The adjusted R^2 and predicted R^2 values for H were 0.9865 and 0.928, respectively. For S, the R^2 values reached 0.993 and 0.961, respectively.

Beside, the distribution of experimental points appears random and follows a normal distribution.[25] These findings validate the robustness and strong compatibility of the proposed model with the experimental results, supporting its application in predicting the synthesis of Ce66 NPs with the dual objective of maximizing both surface area and the yield.

3.2. Morphological characterization of Ce66 NPs synthesized under optimal conditions

Fig. 3a presents the XRD pattern of Ce66 NPs, showing distinct diffraction peaks at 7.3°, 8.4°, 11.9°, 13.8°, 16.9°, 22.2°, and 25.5°, corresponding respectively to the (111), (200), (220), (311), (422), (511), and (600) crystal planes.[18,30] All these reflection planes show a slight shift towards lower 2θ values compared to UiO-66(Zr), which is attributed to the larger ionic radius of Ce^{4+} (0.97 Å) compared to Zr^{4+} (0.84 Å).[31] The XRD pattern with strong peak intensities and clearly defined peak positions indicates the successful formation of Ce66 NPs with high crystallinity.[32]

Fig. 3b and c display the Ce66 NPs SEM picture and particle size distribution, which demonstrate that the particles have a quasi-cubic nanostructure with an average size of 287.63 nm. While some degree of agglomeration was observed, forming secondary structures >600 nm, the uniformity of primary particles suggests effective control over crystal growth. This morphology is advantageous in polymer composite

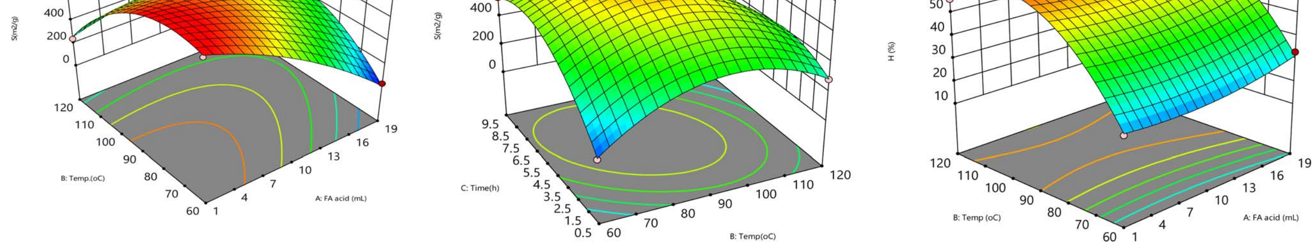

Fig. 1 3D surface plots illustrating the effects of various factors on the surface area of Ce66 NPs: (a) temperature and FA; (b) temperature and time on the surface area and (c) temperature and FA on the yield of Ce66 NPs.

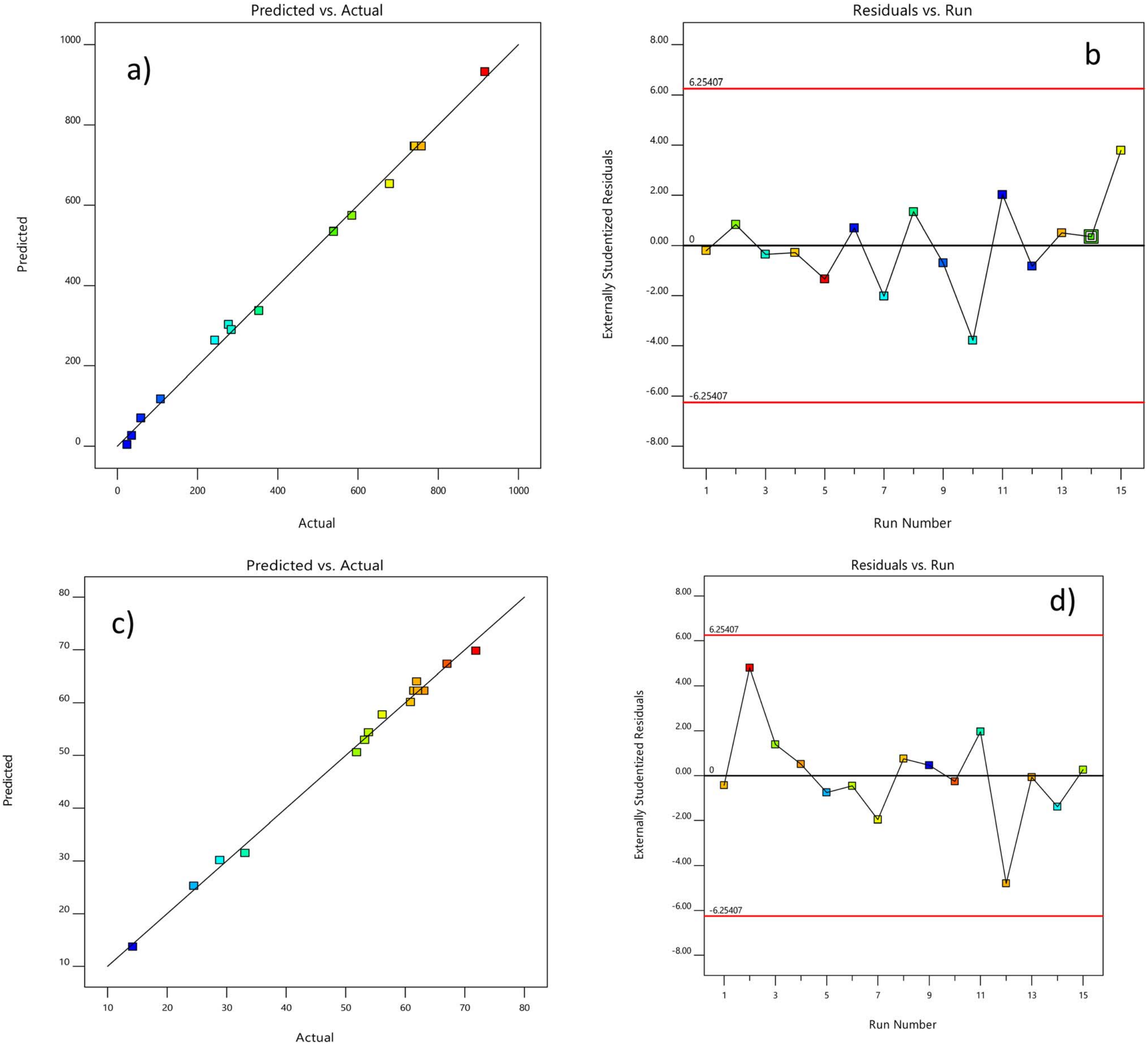

Fig. 2 Experimental *versus* predicted values and random distribution plots of the 15 experimental runs for *S* (a and b) and *H* (c and d).

applications, where well-defined nanoscale geometry can contribute to better particle dispersion, mechanical reinforcement, and interfacial adhesion within the matrix.

Fig. 3d shows the XPS analysis of Ce66 NPs, revealing characteristic peaks at 903.4 eV ($Ce3d_{3/2}$) and 884.8 eV ($Ce3d_{5/2}$) corresponding to Ce^{3+}, along with four additional peaks attributed to Ce^{4+} species. The Ce^{3+}/Ce^{4+} ratio was calculated according to the method reported by Xinyu Wu *et al.*,[33] and found to be 46/54 (%). The coexistence of Ce^{3+} and Ce^{4+} facilitates electron transfer, thereby enhancing the redox capability of Ce66 NPs, making them promising candidates for photocatalytic degradation of persistent organic pollutants.[34] The BET isotherm of Ce66 NPs shows type I behavior, with a high specific surface area of 832.20 $m^2\ g^{-1}$ and a total pore volume of 0.49 $cm^3\ g^{-1}$ (Fig. S1). In comparison to previously published materials, these better surface features demonstrate how well formic acid (FA) works as a modulator to promote controlled nucleation and inhibit aggregation during the synthesis of Ce66 NP.

3.3. Optical properties of Ce66 NPs

The UV_Vis diffuse reflectance spectrum (UV_Vis DRS) of Ce66 NPs was recorded and the results are presented in Fig. 4. As shown in Fig. 4a, the absorption edge attributed to Ce^{4+} is observed around 400 nm, consistent with previous reports.[32] The absorption bands appearing at 250 nm and 320 nm in the UV region correspond to the charge transfer process from O^{2-} (2p) of the BDC ligand to Ce^{4+} (4f).[35] The band gap energy (E_{bg}) of Ce66 NPs (Fig. 4b) determined using the Tauc plot method,[25] is found to be 2.88 eV, which agrees with the findings of Nagarathinam Nagarjun *et al.*[32]

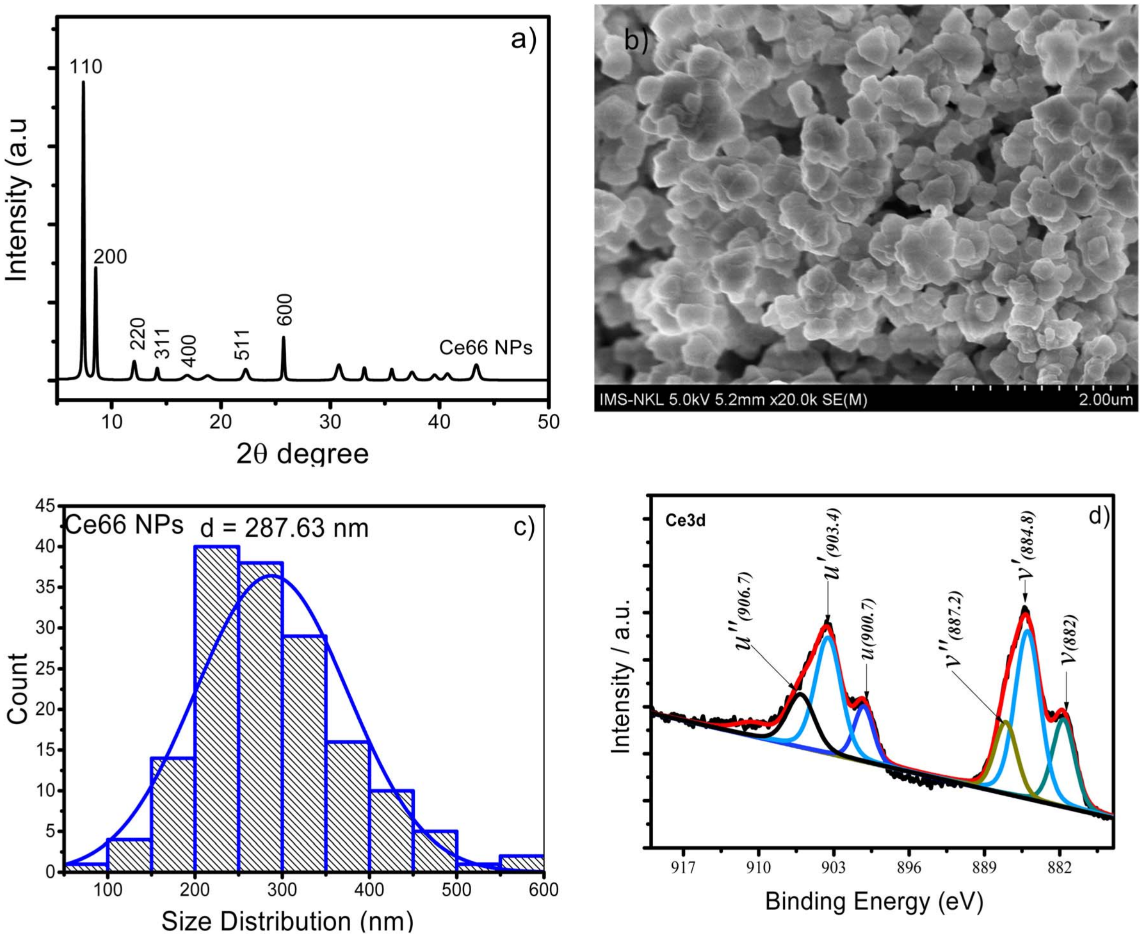

Fig. 3 XRD pattern (a), SEM image and size distribution (b and c), Ce3d XPS spectrum (d) of Ce66 NPs synthesized under optimal conditions.

3.4. Characterization of the properties of starch based films containing Ce66 NPs (SCe*x* with *x* ranging from 0.5 to 3% wt)

3.4.1. Mechanical properties of SCe*x* films. The mechanical properties of biopolymer films are considered among the most critical characteristics, surpassing many other physical properties.[3] The mechanical performance, including tensile strength and elongation at break, was evaluated, and the results are presented in Table 1.

Table 1 demonstrates a clear trend of increasing tensile strength and decreasing elongation at break in nanocomposite films with the increasing content of Ce66 NPs. This mechanical behavior is closely linked to both chemical interactions and physical reinforcement mechanisms provided by the Ce66 NPs. The improvement in tensile strength can be attributed to strong interfacial interactions particularly hydrogen bonding and possible coordination bonding between the abundant hydroxyl

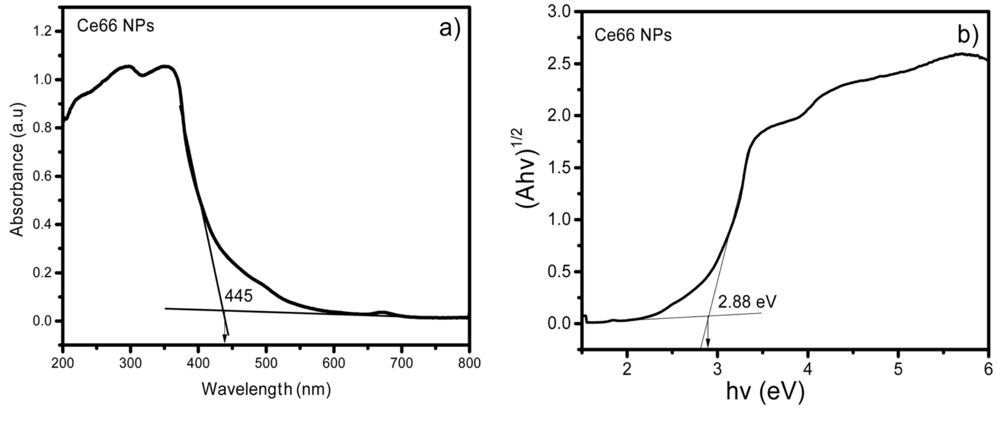

Fig. 4 UV_Vis DRS (a) and E_{bg} (b) of Ce66 NPs.

Table 1 Mechanical properties of SCe*x* films

Biopolymer film	Tensile strength (MPa)	Elongation at break (%)	Film thickness (mm)
SCe0	2.2 ± 0.2	48.3 ± 4.3	0.098 ± 0.002
SCe05	3.2 ± 0.4	44.5 ± 4.1	0.102 ± 0.006
SCe1	8.4 ± 0.8	47.8 ± 2.3	0.101 ± 0.003
SCe3	15.5 ± 0.7	13.5 ± 6.8	0.107 ± 0.005

groups of the starch matrix and the functional groups (carboxylate, hydroxyl) on the Ce66 NPs. The formation of interfacial chemical linkages such as Ce–O–C or Ce–OH–C bridges reinforces the molecular network, resulting in better load transfer efficiency and a stiffer polymer nanoparticle composite. These interactions restrict the mobility of the polymer chains, thus increasing the film's stiffness and mechanical integrity. Additionally, the partially unsaturated 4f orbitals of Ce ions can form coordination complexes with oxygenated groups in the polymer matrix, further contributing to the film's cohesive energy density.[36] However, at higher concentrations (SCe3), the nanoparticles tend to aggregate, creating localized stress points and microstructural inhomogeneities that hinder flexibility and reduce elongation at break.[37] These findings confirm that Ce66 NPs act as anti plasticizing agents in the film matrix, which also leads to a slight increase in the overall thickness of the nanocomposite films as the nanoparticle content increases.

3.4.2. SEM images of SCe*x* films. The surface morphology of the SCe*x* films was examined using SEM method (Fig. 5). As shown in Fig. 5a, the surface of the SCe0 starch film appears smooth, which may be attributed to the effective dispersion of glycerol within the polymer matrix and the complete gelatinization of starch during film formation.[38] The SEM images of SCe05 (Fig. 5b) and SCe1 (Fig. 5c) films reveal a uniform distribution of Ce66 NPs within the film matrix, resulting in films with low surface roughness. This is likely due to the starch forming more stable hydrogen bonds with the MOFs nanoparticles, which leads to stronger interactions between the surface functional groups of the Ce66 NPs and the polymer matrix.[27]

However, at higher nanoparticle concentrations, the surface structure becomes rough, with visible cracks and noticeable agglomeration of Ce66 NPs into clusters (Fig. 5d). This aggregation is thought to be caused by the high surface energy of the nanoparticles, which promotes clustering within the polymer matrix.[39] This phenomenon was also confirmed by Iman Shahabi-Ghahfarrokhi in his study.[40]

3.4.3. Thermogravimetric analysis (TGA) and XRD pattern of SCe*x* films. The thermal stability of the SCe*x* biopolymer films was evaluated using TGA, as shown in Fig. 6a. The results reveal three main stages of thermal decomposition. In the temperature range of 30 to 175 °C, the average weight losses were 14.1%, 10.2%, 8.5%, and 7.8% for SCe0, SCe05, SCe1, and SCe3, respectively. This initial weight loss is attributed to the evaporation of adsorbed moisture through the disruption of hydrogen bonding between water molecules and the material matrix.[41]

The second weight loss stage occurs between 175 °C and 450 °C, corresponding to the glycerol decomposition (190–250 °C) and the degradation of starch molecules. Notably, the biopolymer films exhibited lower weight loss than the neat starch film in this stage, likely due to the breakdown of polymer chains and residual solvents confined within the MOFs nanopores.[42] The incorporation of Ce66 NPs into the biopolymer

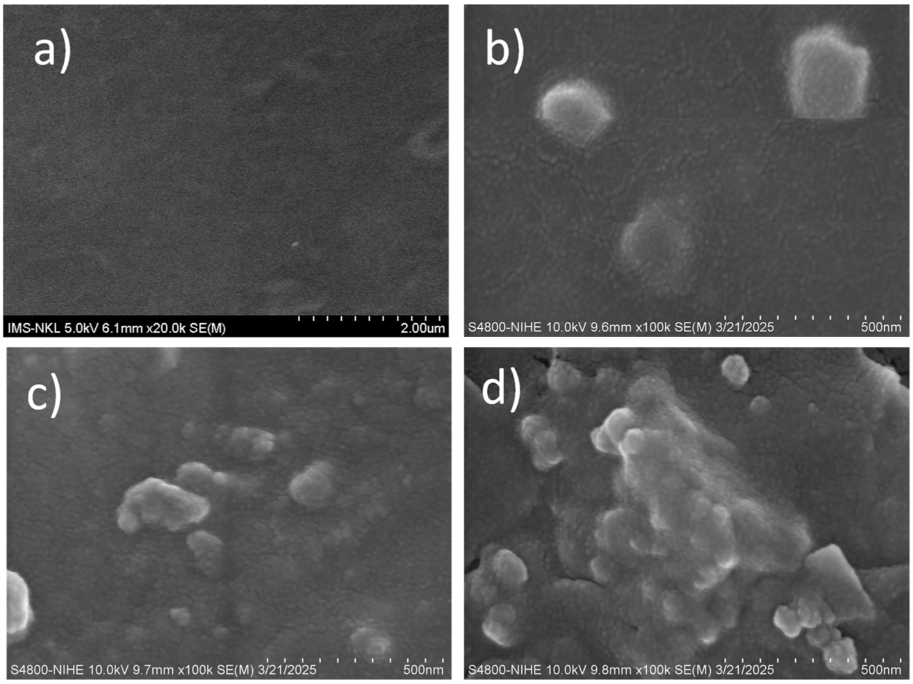

Fig. 5 SEM images of SCe0 (a), SCe05 (b), SCe1 (c), and SCe3 (d) films at different magnifications.

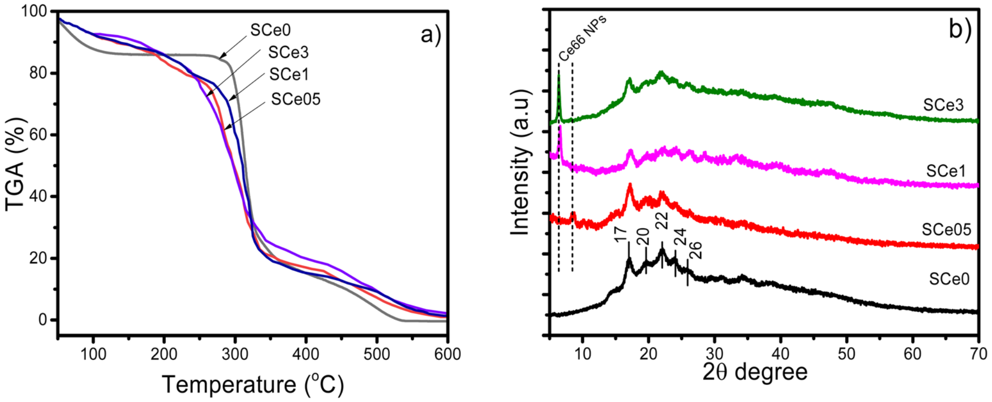

Fig. 6 TGA (a) and XRD patterns (b) of SCe*x* Films.

films acts as a physical barrier and nanofiller that resists structural chain scission caused by thermal stress, thereby retarding the thermal degradation process.[14]

In the third stage (T > 450 °C), thermal cracking of the polymer chains occurs, leading to the formation of carbonaceous species and ash residues. The higher ash content in the biopolymer films compared to the pure starch film can be attributed to the catalytic role of Ce-MOFs in the cracking process, which facilitates the generation of residual carbon.[43,44] These TGA results confirm that Ce66 NPs serve as a protective barrier, enhancing the thermal stability of the biopolymer films.

The XRD patterns of SCe*x* films is presented in Fig. 6b. The XRD pattern of the starch film without Ce66 NPs exhibits broad, low intensity diffraction peaks and a strong amorphous halo, characteristic of semicrystalline polymer materials with low crystallinity. Diffraction peaks at 2θ 17–26° correspond to type B starch crystallinity, indicating interactions between amylose and amylopectin following the gelatinization process.[14]

At Ce66 NPs concentrations below 0.5% wt, the characteristic peaks of Ce66 NPs are almost unobservable due to their high dispersion within the polymer matrix. However, when the Ce66 NPs content increases to 1.0%, the diffraction peaks between 2θ 7–8.5°, typical of the Ce-UiO-66 crystalline structure, reappear.[32] The strong diffraction signals observed in the SCe3 sample indicate a substantial aggregation of Ce66 NPs crystals within the polymer matrix, consistent with the SEM observations.

3.4.4. Water solubility and water vapor permeability of SCe*x* films. The WS of SCe*x* films directly influences their practical applications. Typically, water-insoluble films are preferred for food packaging purposes.[45] The WS and WVP of SCe*x* films are presented in Fig. 7. As shown in Fig. 7a, the starch based film without Ce66 NPs exhibits a high solubility of 22.4%, consistent with several previous reports.[41,45] When Ce66 NPs is incorporated into the biopolymer films, the solubility decreases proportionally with the increasing content of Ce66 NPs, reaching values of 14.4%, 9.6%, and 8.7% for SCe05, SCe1, and SCe3, respectively. This variation in solubility, corresponding to changes in water affinity, is believed to result from strong hydrogen bonding interactions between the polymer matrix and the nanomaterials, which prolong the moisture diffusion path and enhance the rigidity of the biopolymer films.[14,27,46]

The WVP refers to the amount of water vapor passing through the biopolymer films. High WVP is generally undesirable for preserving moisture sensitive products such as pharmaceuticals or dried goods. As seen in Fig. 7b, it can be seen that the pristine starch film exhibited a high WVP value of 2.84 g mm m^{-2} d^{-1} kPa^{-1}, which is attributed to the presence of hydrophilic plasticizers such as glycerol acting as hydrocolloids that enhance water vapor permeability.[47] Upon the incorporation of Ce66 NPs, the WVP decreased and reached 2.25 (SCe05), 1.69 (SCe1), and 1.81 g mm m^{-2} d^{-1} kPa^{-1} (SCe3), respectively.

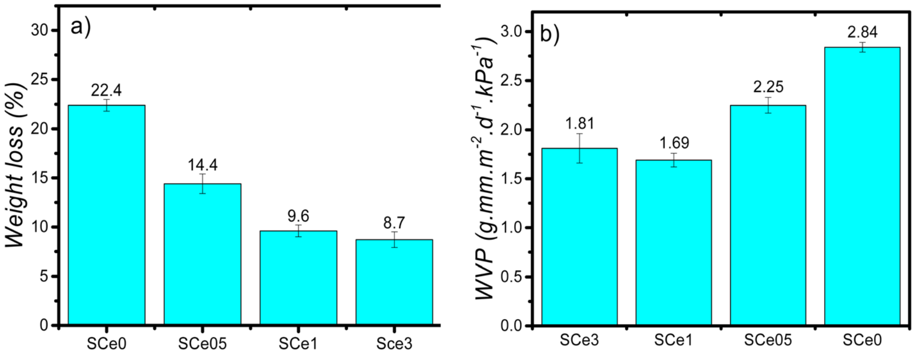

Fig. 7 WS (a) and WVP (b) of SCe*x* films.

The observed increase in WVP between SCe3 and SCe1 is attributed to the excessive presence of porous nanoparticles, which disrupted the dense film structure and accelerated water molecule penetration through capillary channels within the polymer matrix.[27] The nanoparticles acted as hydrophobic agents, increasing the tortuous pathway for water diffusion and thereby reducing WVP. Similar observations have also been reported in previous studies.[48,49]

3.4.5. Transparency, opacity, and UV-blocking properties of SCe*x* films. Transparency, opacity, and UV-blocking properties of SCe*x* films are presented in Fig. 8. The optical properties of the films are represented by their light transmittance and opacity (Fig. 8a). The initial starch film exhibited a relatively high transparency of 70.33%, which is greater than that of other biopolymers such as PLA, chitosan, and cellulose, as well as compared to other modified starch based films.[1,44,50] As shown in Fig. 8a, *T*% value showed a decreasing trend with increasing concentrations of Ce66 NPs, with transmittance values of 55.55%, 29.4%, and 9.6% for SCe05, SCe1, and SCe3, respectively. This decline is attributed to the dependence of opacity on nanoparticle concentration and film thickness, as also illustrated in Fig. 8a. The UV-vis transmittance spectrum and opacity values of SCe0 to SCe3 films, measured in the wavelength range of 200 nm to 800 nm, are shown in Fig. S2a and S2b. The opacity increased from 7.49 mm^{-1} to 16.59 mm^{-1} with higher Ce66 NPs loading. SEM results and opacity measurements confirmed that better filler dispersion within the starch matrix corresponds to higher transparency of the synthesized starch films.

Fig. 8b illustrates the influence of Ce66 NPs concentration on the UV-blocking capabilities of the biopolymer films, particularly for UVA, UVB, UVC, and blue light. The SCe*x* films demonstrated complete (100%) blocking of UVC radiation. The SCe0 film blocked 61.25% of UVA and 35.65% of UVB, and 30.5% of blue light, respectively. These values improved with the inclusion of Ce66 NPs at varying concentrations. Specifically, UVA blocking efficiency increased from 83.5% to 100% in SCe05, SCe1, and SCe3. UVB shielding also improved, reaching 68.12% and 95.6% in SCe05 and SCe1, respectively. Notably, the SCe3 film blocked both UVB and blue light at 100% and 97.2%, respectively.

However, SCe3 exhibited a high opacity of 16.50 mm^{-1}, along with nanoparticle aggregation and membrane fracture, as observed in SEM images, significant reducing in elongation percentage. Therefore, it is unsuitable for food packaging applications. The UV-blocking mechanism is associated with the light absorption properties and the E_{bg} of Ce66 NPs, as demonstrated in Fig. 4. Upon light absorption, Ce66 NPs trap the light and generate photoexcited electrons and holes at higher energy states, thereby reducing the amount of UV radiation reaching the SCe*x* films.[1]

In general, films lacking UV-blocking capabilities may accelerate oxidative degradation, leading to nutrient loss in preserved food and negatively affecting the stability of organic materials (*e.g.*, discoloration and degradation).[51] Therefore, the SCe*x* films, exhibiting excellent UV-blocking performance, show great potential for protective applications in food packaging and optoelectronic devices. Comparative evaluations with previously reported packaging films are summarized in Table 2.

Among the nanocomposite films containing nanoparticles summarized in Table 2, the starch-based biofilm incorporating Ce66 NPs demonstrates a unique combination of enhanced UV-blocking and excellent water vapor permeability properties, making it a highly promising material for food packaging applications. Compared to other nanofillers, the SCe1 film achieved superior UV-blocking performance, effectively shielding 83.5% of UVA, 95.6% of UVB, and 100% of UVC radiation significantly outperforming ZnO-based films, which reached a maximum UVB shielding efficiency of 81%. In terms of WVP characteristics, the SCe1 film exhibited one of the lowest WVP values (1.69 $\text{g mm m}^{-2}\ \text{d}^{-1}\ \text{kPa}^{-1}$), surpassing even halloysite nanotube and graphite oxide based composites, which are known for their barrier performance. According to the Chinese standard (BB/T 0041-2021), the acceptable WVP value for packaging materials is less than 6.0 g $(\text{m}^2\ 24\ \text{h})^{-1}$. The WVP of the film obtained in the present study was 1.69 $\text{g mm m}^{-2}\ \text{d}^{-1}$

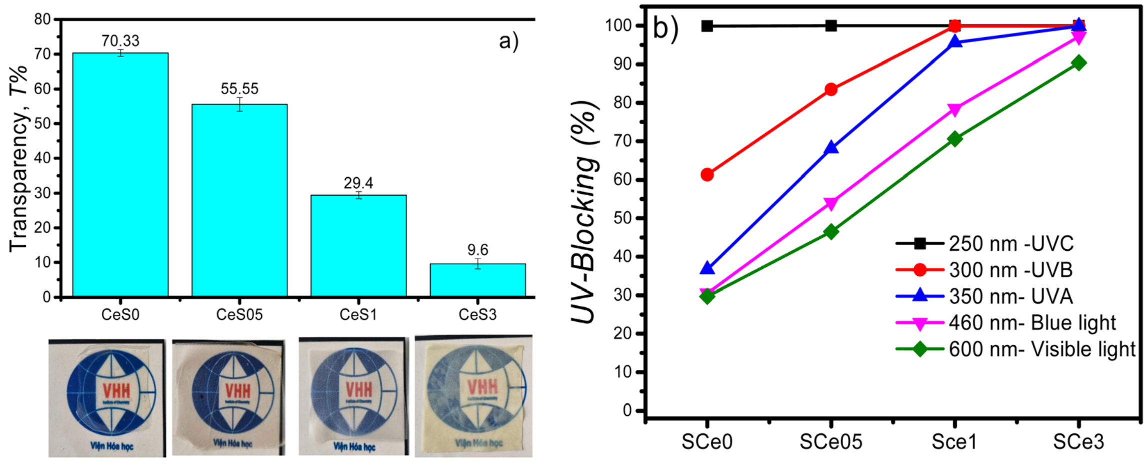

Fig. 8 Transparency (a) and UV-blocking ability (b) of SCe*x* films.

Table 2 Specifics of the nanomaterials that are required to create nano-enhanced bioplastics and their improved characteristics

Reinforced nanomaterials	Biopolymers or polymers	Mechanical properties		UV-blocking	WVP	Enhanced functionalities	References
		Tensile strength	Elongation at break				
Silver nanoparticle	Cassava starch	4.2 MPa	4.7%	Not specified	Not specified	Non-toxicity to fibroblast cells	52
ZnO	Starch/agar	5.331 MPa to 7.459 MPa	32.178 to 55.771%	63.1% to 67.78% UVA 74.5% to 81% UVB	Not specified		53
Halloysite nanotube	Starch	3.5 MPa to 5.73 MPa	25 to 40%	Not specified	1.89 to 3.07 g mm m^{-2} d^{-1} kPa^{-1}	Excellent flame retardancy	54
Graphite oxide carbon	Starch	2.1 Mpa to 21.7 Mpa	45.73 to 59.87%	Not specified	3.86 to 3.27 g mm m^{-2} s^{-1} kPa^{-1}		55
NH_2-UiO-66	Corn starch, gellan gum	28.5 MPa to 31.8 MPa	25% to 16%	Not specified	2.98 g mm m^{-2} d^{-1} kPa^{-1}	Antibacterial	39
Ce66 NPs	Starch	2.2 MPa to 8.4 MPa	47.8 to 48.3%	83.5% UVA 95.6% UVB 100% UVC	1.69 g mm m^{-2} d^{-1} kPa^{-1}	Ce-UiO-66 was capable of degrading 65% of RR195 dye	This work

kPa^{-1}, which corresponds to 40.14 g (m^2 24 $h)^{-1}$, a relatively high value. However, the WVP of the film developed in this study was found to be better than that of several previously reported biopolymer-based films.[56] Furthermore, the tensile strength of the SCe1 film increased markedly from 2.2 MPa to 8.4 MPa, indicating strong reinforcement while still maintaining appropriate flexibility.

Beyond its use as a reinforcing nanofiller, Ce66 NPs also demonstrated independent photocatalytic activity, which allowed them to degrade up to 65% of the reactive dye RR195 in the presence of sunlight (Fig. S3 to S5). This multifunctionality, along with the enhanced UV resistance and water barrier properties, highlights the considerable potential of Ce66 NPs for advanced food packaging solutions.

4. Conclusions

The study successfully synthesized Ce-UiO-66 MOFs nanoparticles with high crystallinity, an average particle size of approximately 287 nm, a large specific surface area (832.2 m^2 g^{-1}), and the yield of 66.25%. Analysis based on the RSM-BBD model revealed that FA concentration and temperature had the most significant influence on the yield. In contrast temperature and reaction time were the primary factors affecting surface area.

Ce66 NPs not only enhanced the removal efficiency in degrading RR195 dye under sunlight (65%) but also significantly improved the physicomechanical properties of starch based biopolymer films. Specifically, the SCe1 film demonstrated outstanding UV-blocking capability, blocking 83.5%, 95.6%, and 100% of UVA, UVB, and UVC radiation, respectively far superior to starch films without nanoparticles. Regarding of mechanical properties, the tensile strength of the films increased from 2.2 MPa (SCe0) to 15.5 MPa (SCe3), indicating substantial reinforcement due to the incorporation of Ce66 NPs. Furthermore, the water solubility of the films was reduced threefold, and the water vapor absorption capacity decreased to 1.69 g mm m^{-2} d^{-1} kPa^{-1}, which corresponds to 40.14 g (m^2 24 $h)^{-1}$, demonstrating improved stability in humid environments for the SCe*x* films containing Ce66 NPs.

These findings confirm the dual functional potential of Ce66 NPs as efficient photocatalysts for environmental pollutant treatment and as ideal nanofillers to enhance the mechanical and UV-blocking properties of biopolymer films thus opening new avenues for developing environmentally friendly food packaging materials.

Author contributions

Giang H. Le: project administration, methodology, supervision, writing-original draft. Duong A. Thanh: data curation, formal analysis, software. Trang T. T. Pham: conceptualization, methodology, funding acquisition. Quang Vinh Tran: investigation, formal analysis. Nhiem Ngoc Dao: writing-review & editing, software. Kien Trung Nguyen: resources, investigation. Son Tung Pham: visualization, data analysis. Trang T. T. Quan: validation, supervision, writing-review & editing.

Conflicts of interest

The authors declare no competing financial interests or personal relationships that could have influenced the work reported in this study.

Data availability

The datasets generated and analyzed during this study are available from the corresponding author upon reasonable request.

Supplementary information is available. See DOI: **https://doi.org/10.1039/d5ra03117f**.

Acknowledgements

The authors would like to express their sincere thanks to project CSCL06.03/24-25 for providing financial support for this research.

References

1 M. L. Rojas, D. Asmat-Campos, A. Carreño-Ortega and N. Raquel-Checca, *Int. J. Biol. Macromol.*, 2024, **282**, 137468.
2 J. Jin, B. Luo, S. Xuan, P. Shen, P. Jin, Z. Wu and Y. Zheng, *Int. J. Biol. Macromol.*, 2024, **266**, 131253.
3 A. Ancy, M. Lazar, A. Saritha Chandran and M. Ushamani, *Sustainable Chem. Pharm.*, 2024, **37**, 101377.
4 Z. Alves, N. M. Ferreira, P. Ferreira and C. Nunes, *Carbohydr. Polym.*, 2022, **291**, 119517.
5 C. Li, X. Zhang, H. Chen, H. Wang, J. Huang, T. Li, S. Wang and W. Dong, *Int. J. Biol. Macromol.*, 2025, **295**, 139567.
6 M. Jiménez-Rosado, E. Bouroudian, V. Perez-Puyana, A. Guerrero and A. Romero, *J. Cleaner Prod.*, 2020, **262**, 121517.
7 M. R. Amin, M. A. Chowdhury and M. A. Kowser, *Heliyon*, 2019, **5**, e02009.
8 O. Oluwasina, A. Aderibigbe, S. Ikupoluyi, O. Oluwasina and T. Ewetumo, *Sustain. Chem. Environ.*, 2024, **6**, 100093.
9 G. H. Le, D. A. Thanh, P. T. H. My, T. T. T. Pham, T. T. T. Quan, T. N. Nguyen, Q. K. Nguyen and Q. A. Ngo, *Mater. Res. Express*, 2023, **10**, 015001.
10 N. A. Khan, M. B. Niazi, F. Sher, Z. Jahan, T. Noor, O. Azhar, T. Rashid and N. Iqbal, *Polymers*, 2021, **13**, 2307.
11 S. El Hankari, M. Bousmina and A. El Kadib, *Prog. Mater. Sci.*, 2019, **106**, 100579.
12 A. Maraddi, M. Halakarni, M. Manohara Halanur and S. K. Nataraj, *Sustainable Mater. Technol.*, 2023, **35**, e00537.
13 L. Sun, L. Li, X. An and X. Qian, *Polymers*, 2021, **13**, 2433.
14 S. Jafarzadeh, M. Golgoli, M. Azizi-Lalabadi, J. Farahbakhsh, M. Forough, N. Rabiee and M. Zargar, *Int. J. Biol. Macromol.*, 2024, **265**, 130899.
15 A. Balakrishnan, M. M. Jacob, N. Dayanandan, M. Chinthala, M. Ponnuchamy, D.-V. N. Vo, S. Appunni and A. S. Gajendhran, *Mater. Adv.*, 2023, **4**, 5920–5947.
16 L. A. M. Mahmoud, R. Telford, T. C. Livesey, M. Katsikogianni, A. L. Kelly, L. R. Terry, V. P. Ting and S. Nayak, *ACS Appl. Bio Mater.*, 2022, **5**, 3972–3981.
17 H. Molavi, *Coord. Chem. Rev.*, 2025, **527**, 216405.
18 M. Lammert, M. T. Wharmby, S. Smolders, B. Bueken, A. Lieb, K. A. Lomachenko, D. D. Vos and N. Stock, *Chem. Commun.*, 2015, **51**, 12578–12581.
19 J. Jacobsen, A. Ienco, R. D'Amato, F. Costantino and N. Stock, *Dalton Trans.*, 2020, **49**, 16551–16586.
20 A. Mancuso, O. Tammaro, F. Raffone, G. Cicero, O. Sacco, M. Pansini, V. Vaiano and S. Esposito, *Chem. Eng. J.*, 2025, **504**, 158698.
21 C. R. Marshall, S. A. Staudhammer and C. K. Brozek, *Chem. Sci.*, 2019, **10**, 9396–9408.
22 J. Lai, W. Niu, R. Luque and G. Xu, *Nano Today*, 2015, **10**, 240–267.
23 J. M. Yassin, A. M. Taddesse and M. Sánchez-Sánchez, *Microporous Mesoporous Mater.*, 2021, **324**, 111303.
24 Z. Tu, X. He, X. Du, W. Li, D. Wang, W. Fang, H. Zhang, H. Chen, L. Zhao and C. Wang, *Chem. Eng. J.*, 2025, **505**, 159357.
25 G. H. Le, D. A. Thanh, T. T. T. Pham, Q. V. Tran, N. N. Dao, K. T. Nguyen and T. T. T. Quan, *RSC Adv.*, 2025, **15**, 7078–7089.
26 L. V. Aguiar de Oliveira, N. R. Checca Huaman, S. N. Monteiro, U. O. Costa and L. Vitorazi, *J. Mater. Res. Technol.*, 2025, **35**, 2736–2754.
27 S. Dhiman, A. Kumari, S. Kumari and R. Sharma, *J. Environ. Chem. Eng.*, 2025, **13**, 116296.
28 J. Zhao, Y. Wang and C. Liu, *Food Anal. Methods*, 2022, **15**, 2840–2846.
29 J. Yuan, W. Xu, Y. Wang, S. Wang, R. Hao, Y. Dong, Q. Li and Y. Zhao, *Mater. Sci. Eng., B*, 2025, **311**, 117800.
30 X. Hou, Y. Bian and L. Yang, *Microporous Mesoporous Mater.*, 2022, **345**, 112214.
31 M. Stawowy, M. Róziewicz, E. Szczepańska, J. Silvestre-Albero, M. Zawadzki, M. Musioł, R. Łuzny, J. Kaczmarczyk, J. Trawczyński and A. Łamacz, *Catalysts*, 2019, **9**, 309.
32 N. Nagarjun, M. Jacob, P. Varalakshmi and A. Dhakshinamoorthy, *Mol. Catal.*, 2021, **499**, 111277.
33 X. Wu, L. Fan, J. Zhang, L. Wang, L. Cao, H. Chen and L. Yi, *J. Alloys Compd.*, 2025, **1017**, 179158.
34 H. Zhang, J. Ye, Y. Dai, H. Yang, J. Zhang, Y. Xie and W. Zhang, *Chem. Eng. J.*, 2024, **502**, 158240.
35 E. E. Ghadim, M. Walker and R. I. Walton, *Dalton Trans.*, 2023, **52**, 11143–11157.
36 F. Gapsari, S. N. K. Andrianto, A. Harmayanti, A. M. Sulaiman, C. W. Kartikowati, K. A. Madurani, W. Wijayanti, S. M. Rangappa and S. Siengchin, *Int. J. Biol. Macromol.*, 2025, **290**, 138571.
37 D. R. Adhika, G. Genecya, A. A. Habibah, A. N. A. R. Putri and U. S. F. Arrozi, *OpenNano*, 2025, **22**, 100234.
38 R. Anitha, K. Jayakumar, G. V. Samuel, M. E. Joice, M. Sneha and D. S. Seeli, *Eng. Proc.*, 2024, **61**, 30.
39 K. Zhang, D. Jin, X. Guo, C. Shu, H. Ouyang, Y. He, K. Tang, P. Zhu, Y. Wang and H. Li, *Ind. Crops Prod.*, 2024, **220**, 119205.

40 I. Shahabi-Ghahfarrokhi, F. Khodaiyan, M. Mousavi and H. Yousefi, *Int. J. Biol. Macromol.*, 2015, **77**, 85–91.
41 B. Nayak, P. Jain, L. Kumar, A. A. Mishra and K. K. Gaikwad, *Int. J. Biol. Macromol.*, 2024, **267**, 131545.
42 S. Lee, Y. Lei, D. Wang, C. Li, J. Cheng, J. Wang, W. Meng and M. Liu, *Polymers*, 2019, **11**, 1986.
43 Y. Wu, C. Yao, Y. Hu, X. Zhu, Y. Qing and Q. Wu, *Materials*, 2014, **7**, 637–652.
44 W. Homthawornchoo, P. Kaewprachu, S. Pinijsuwan, O. Romruen and S. Rawdkuen, *Polymers*, 2022, **14**, 2505.
45 I. Choi, D. Shin, J. S. Lyu, J.-S. Lee, H.-g. Song, M.-N. Chung and J. Han, *Food Packag. Shelf Life*, 2022, **33**, 100867.
46 S. Feng, Q. Tang, Z. Xu, K. Huang, H. Li and Z. Zou, *Food Hydrocolloids*, 2023, **135**, 108193.
47 A. A. Al-Hassan and M. H. Norziah, *Food Hydrocolloids*, 2012, **26**, 108–117.
48 J. Liu, J. Huang, Z. Hu, G. Li, L. Hu, X. Chen and Y. Hu, *Int. J. Biol. Macromol.*, 2021, **189**, 363–369.
49 A. H. D. Abdullah, O. Dwi Putri, A. K. Fikriyyah, R. C. Nissa, S. Hidayat, R. Firman Septiyanto, M. Karina and R. Satoto, *Polym.-Plast. Technol. Mater.*, 2020, **59**, 1259–1267.
50 S. Ni, H. Bian, Y. Zhang, Y. Fu, W. Liu, M. Qin and H. Xiao, *Biomacromolecules*, 2022, **23**, 829–838.
51 Y. Qian, C. Qin, J. Zhang, B. Shi, Y. Wei, C. Wang, J. Niu, S. Kang, G. Chen and Y. Liu, *Int. J. Biol. Macromol.*, 2025, **299**, 140130.
52 C.-C. Liu, Y.-H. Hsieh, P.-F. Lai, C.-H. Li and C.-L. Kao, *Dyes Pigm.*, 2006, **68**, 191–195.
53 N. Ninan, B. Pidhatika, R. Bright, B. M. Kartika, R. P. Rudianto, Y. A. Swasono, R. Ardhani and K. Vasilev, *J. Mater. Sci.*, 2024, **59**, 9003–9020.
54 Y. Liu, J. Wang, H. Yue, Z. Du, X. Cheng, H. Wang, F. Cheng and X. Du, *Carbohydr. Polym.*, 2024, **323**, 121465.
55 C. Geng, Z. Zhang, R. Lin, L. Guo, P. Liu, C. Yuan, Y. Fang and B. Cui, *Ind. Crops Prod.*, 2023, **195**, 116404.
56 S. Jia, Y. Sun, Y. Hou, S. Cheng, W. Su, M. Tan and H. Wang, *Chem. Eng. J.*, 2025, **514**, 163445.